In-plane graphene/boron-nitride heterostructures as an efficient metal-free electrocatalyst for the oxygen reduction reaction

Qiao Sun
Soochow University, qsun@uow.edu.au

Caixia Sun
East China University of Science and Technology

Aijun Du
Queensland University of Technology

S X. Dou
University of Wollongong, shi@uow.edu.au

Zhen Li
University of Wollongong, zhenl@uow.edu.au

In-plane graphene/boron-nitride heterostructures as an efficient metal-free electrocatalyst for the oxygen reduction reaction

Abstract

Exploiting metal-free catalysts for the oxygen reduction reaction (ORR) and understanding their catalytic mechanisms are vital for the development of fuel cells (FCs). Our study has demonstrated that in-plane heterostructures of graphene and boron nitride (G/BN) can serve as an efficient metal-free catalyst for the ORR, in which the C-N interfaces of G/BN heterostructures act as reactive sites. The formation of water at the heterointerface is both energetically and kinetically favorable via a four-electron pathway. Moreover, the water formed can be easily released from the heterointerface, and the catalytically active sites can be regenerated for the next cycle. Since G/BN heterostructures with controlled domain sizes have been successfully synthesized in recent reports (e.g. Nat. Nanotechnol., 2013, 8, 119), our results highlight the great potential of such heterostructures as a promising metal-free catalyst for the ORR in FCs.

Disciplines

Engineering | Physical Sciences and Mathematics

Publication Details

In-plane Graphene/Boron-Nitride Heterostructure as Efficient Metal-Free Electrocatalyst for the Oxygen Reduction Reaction

Qiao Sun,[a] Caixia Sun,[b] Aijun Du,[c] Shixue Dou,[d] and Zhen Li*[a,d]

Exploiting metal-free catalysts for the oxygen reduction reaction (ORR) and understanding their catalytic mechanisms are vital for the development of fuel cells (FCs). Our study has demonstrated that in-plane heterostructures of graphene and boron nitride (G/BN) can serve as an efficient metal-free catalyst for the ORR, in which the C-N interfaces of G/BN heterostructures act as reactive sites. The formation of water at the heterointerface is both energetically and kinetically favorable via a four-electron pathway. Moreover, the water formed can be easily released from the heterointerface, and the catalytically active sites can be regenerated for the next cycle. Since G/BN heterostructures with controlled domain sizes have been successfully synthesized in recent reports (e.g. Nat. Nanotechnol., 2013, 8, 119), our results highlight the great potential of such heterostructures as a promising metal-free catalyst for ORR in FCs.

Introduction

Fuel cells (FCs) have been considered to be one of the best alternatives to traditional energy resources because of their high efficiency and low emissions.[1, 2] The oxygen reduction reaction (ORR) is a critical process in FCs, which is normally catalyzed on cathodes by noble platinum catalyst. The high cost and less abundance, poor stability, sluggish reaction kinetics, and deactivation by CO poisoning that characterize platinum catalyst have hindered the large-scale application of FCs. There are increasing worldwide research efforts to search for low cost and high performance non-precious metal or metal-free catalysts for the ORR.[3, 4]

Low dimensional metal-free nanomaterials, such as carbon and boron nitride (BN) based materials have been studied extensively because of their fascinating properties and applications.[5-11] Although the sp^2 carbon nanomaterials have abundant free-flowing π electrons, these π electrons are too inert to be directly used in the ORR. In recent years, it has been revealed that the π electrons of carbon atoms in B doped, N doped, and their co-doped carbon nanomaterials can be activated by conjugating with the lone-pair electrons from N dopants with the assistance of the low electronegativity of B atoms, and the substrate.[4, 12-22] These dopants and their doping manners play important roles in catalyzing the ORR, and determine the catalysis mechanisms.[12-18, 22] For example, Hu's group demonstrated that the separated B and N co-doped carbon nanotubes have excellent ORR performance, and the bonded B and N co-doped analogues (in which B and N

dopants form bonds) exhibit a totally different performance.[17] For BN nanomaterials, their wide band gaps ranging from 3.6–7.1 eV (depending on the experimental method) limit the efficient electronic communication, and they cannot be directly used as effective metal-free catalysts for the ORR. Recent studies have demonstrated that their band structures can be manipulated by introduction of appropriate defects (B and N vacancies and impurities) and substrates to improve activation for the ORR.[23, 24] It is a challenge, however, to precisely control the dopant behavior, doping efficiency, and level of defects during their synthesis, and their catalytic efficiency needs to be further improved.

Hybridized graphene/BN (G/BN) nanomaterials are different from pure BN, pure carbon, and their doped analogues, because they combine the properties of the two disparate materials with similar lattice parameters and crystal structure, which have unique structural features, dramatically different physical and chemical properties, such as band edge opening, magnetism, unique thermal transport and robust half-metallic behavior for diverse applications.[25-39] Since Ci's first pioneering work of obtaining a few layers of heterostructure of graphene (G) and h-BN,[26] atomic layers of hybridized G/BN heterostructures have attracted great attention. The fabrication of monolayer G/BN is very challenging, although researchers have recently made great progress in the synthesis of various G/BN heterostructures on different substrates, such as Cu foil,[28] Ru(0001),[32] Rh(111),[30] Ir(111),[33] Pt(111),[39] etc., which have promoted studies of their applications, especially as metal-free catalysts for the ORR.

Although the interfaces play a key role in the catalysis of above mentioned hybridized G/BN nanomaterials, their size effect and performance towards the ORR are as yet unknown. In this report, we have demonstrated three major processes of ORR on the various of heterostructures through a comprehensive theoretical study for the first time, including (1) the size dependence of O_2 adsorption on interfaces of the heterostructured G/BN nanoribbons, (2) the reaction of O_2 on the heterointerfaces of G/BN nanoribbons, and (3) the desorption of water molecules from the heterointerfaces of G/BN nanoribbons. The results show that G/BN interfaces can dramatically boost the activity towards the ORR, supported by results from frontier molecular orbital analyses that the interface areas have higher reactivity and higher conductivity. Moreover, the water molecules formed in the reaction is easily released from the G/BN catalyst, and the interfacial active sites can be reused for the next cycle. The high-performance and low-cost of G/BN heterostructures will promote experimental exploitation of their application as novel metal-free electrocatalyst for ORR in FCs.

Results and discussion

It has known that neither pure carbon nor BN nanomaterials can directly serve as efficient catalysts towards the ORR. Their performance can be significantly improved by chemical doping, and varied with position and distribution of dopants, e.g. separated B and N co-doped carbon nanotubes exhibit better catalytic activity towards ORR than bonded B and N co-doped counterparts and undoped carbon nanotubes.[17] This is due to the separation of B and N dopants which can prevent neutralization between them, and they remain capable of conjugating with the carbon π system as in the sole doped case. Such irregular and peculiar behaviour of co-doped materials with respect to the ORR was also described by Wang et al..[12, 13] However, there is no report on the hybrid G/BN nanomaterials (in which the B and N dopants are bonded) with heterointerfaces as efficient catalysts towards the ORR, which we investigate in the current manuscript.

Up to now, there are three hybrid G/BN interfaces obtained experimentally on different substrates, and they are the h-armchair G/BN interface, the zigzag N-C interface, and the zigzag B-C interface. Previous studies have revealed that the type of boundary with zigzag G/BN interfaces are preferable on some metal substrates, such as Cu foil,[28] Rh(111),[30] Ru(0001),[32] Ir(111)[33]. In addition, their electronic properties and activities are strongly dependent on their crystallographic orientations and feature sizes.[29, 36] In order to address this issue, we have investigated O_2 adsorption on the two zigzag G/BN nanomaterials with N-C and B-C interfaces (Figure 1), respectively. Our results indicate that O_2 molecules can only participate in a strong interaction on the zigzag G/BN with a C-N interface. The strong interaction of O_2 molecules with C-N interfaces in zigzag G/BN nanoribbons can be understood through band structure analysis. We have calculated the band structure for a G/BN nanoribbon with a C-N interface and

plotted it in Figure 2(a). The charge densities of valence band maximum (VBM) and conduction band minimum (CBM) of the G/BN nanoribbon at the Gamma point are shown in Figure 2(b) and (c). The presence of CBM at the heterointerface indicates that the interface has higher reactivity and conductivity. Therefore, zigzag G/BN nanoribbons with a C-N interface were selected as a simple model to study the size dependence of O_2 adsorption.
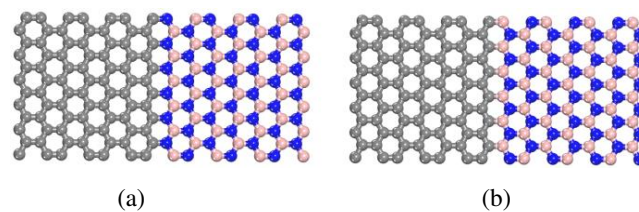

Figure 1. In-plane zigzag G/BN heterostructure with (a) C-N and (b) C-B interfaces. Atom color code: blue, nitrogen; pink, boron; gray, carbon.
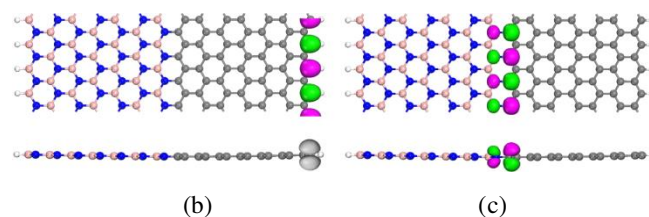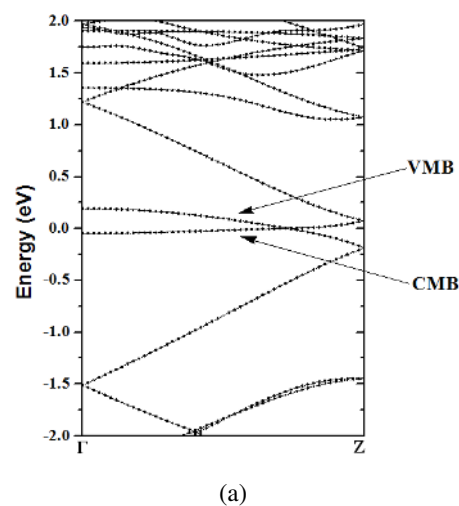

(a)

Figure 2. The band structure for G/BN nanoribbon (a), and top and side views of charge density for (b) valence band maximum (VBM) and (c) conduction band minimum (CBM) of G/BN nanoribbon at the Gamma point. The isosurface value is $0.03e/\text{Å}^3$. Atom color code: blue, nitrogen; pink, boron; gray, carbon; white, hydrogen.
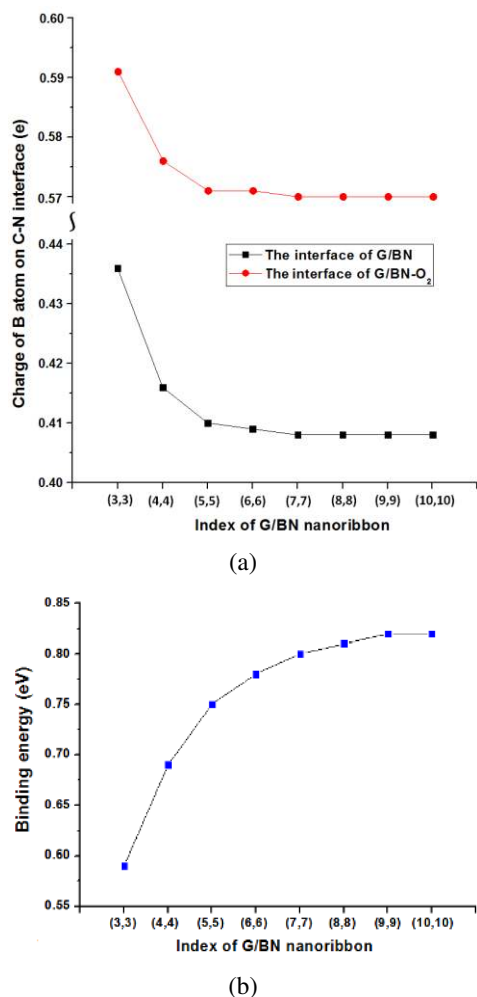
(a)

(b)

Figure 3. (a) Mulliken charge distribution (e) of B atoms for different sizes of G/BN and G/BN-O₂ nanoribbons, and (b) binding energy (eV) of O₂ adsorption on different sizes of G/BN nanoribbons.

Figure 3 and Table S1 in the supporting information present the Mulliken charge distributions of important atoms in the C-N interfaces of G/BN nanoribbons with different sizes, as well as the important structural parameters, charge transfers from nanoribbons to O_2 molecules, and the binding energies (eV) of the chemisorption of O_2 on these materials. The gas phase O_2 used in this study is in its triplet state. The zigzag G/BN(n,n) nanoribbons on graphene and BN sides are classified by the number of the graphene and BN zigzag chains across the ribbon width, as shown in Figure S1 in the supporting information. The results clearly show that the positive charges on boron atoms in the C-N interfaces decrease as the nanoribbon size increases from G/BN (3,3) to G/BN (7,7). In detail, the Mulliken charge distribution on boron atoms decreases from 0.436 e to 0.408 e when the size of the nanoribbon increases from 13.771 Å (G/BN (3,3)) to 31.051 Å (G/BN (7,7)), which means that it becomes easier for the boron atoms to donate negative charge to O_2 with increasing size of the nanoribbon. The charge transfer from the nanoribbon to O_2 with the chemisorption of O_2 on the C-N interface of the nanoribbon

changes from -0.475 e to -0.496 e as the size of nanoribbons increases from G/BN (3,3) to G/BN (7,7). The values of the charge transfer also prove the above analysis.

When the size of the nanoribbons increases from 35.374 Å (G/BN (8,8)) to 44.013 Å (G/BN (10,10)), the charge distribution of boron atoms on the interfaces remains constant (0.408 e), which indicates that the activities at the interfaces of large nanoribbons are independent on their size. The values of charge transfer are also consistent with the above results, and they are almost constant (from -0.498 e to -0.500 e) when the nanoribbon size increases from G/BN (8,8) to G/BN (10,10). For the chemisorbed configurations (Table 1), the O-O distances in all structures increase from 1.225 Å (in the gas phase) to the range of 1.422−1.434 Å (chemisorbed configurations), and the two new B-O bonds formed between O_2 and the G/BN nanoribbons are in the range of 1.566−1.576 Å for all the different sizes of nanoribbons. Moreover, in the configurations from G/BN (3,3) to G/BN (7,7), the O-O distance increases with increasing size of the nanoribbons, and then remains constant with further increasing size of the G/BN nanoribbon. Similarly, the B-O distance increases as the G/BN nanoribbon increases in size from G/BN (3,3) to G/BN (7,7), and remains constant for the remaining bigger sized nanoribbons. The geometrical properties also support that the interactions between O_2 and the G/BN nanoribbons initially increase with increasing G/BN size, but it remains almost constant as the size of the G/BN nanoribbons further increases. The dependence of binding energies on the size of G/BN nanoribbons are shown in Figure 3(b), which shows that the binding energies for O_2 adsorption on G/BN nanoribbons increase from 0.59 eV to 0.80 eV when the size of the nanoribbons increases from G/BN (3,3) to G/BN (7,7), but then remain almost constant with values around 0.081—0.082 eV when the size of the nanoribbon further increases. Moreover, we also have investigated the size dependence of graphene nanoribbons and BN parts of the binding energies of O_2 adsorption on the interfaces of G/BN. The detail information has been listed in Table S2 in the supporting information. From the calculational results we can see that the binding energies of O_2 adsorption on the G/BN interfaces are much more sensitive to the width of graphene nanoribbons and only weakly depend on the size of BN parts, which can be explained from the point view of the charge distributions of these chemisorbed configurations. The above results clearly demonstrate the size effects of G/BN nanoribbon for adsorption of O_2, and provide a very clear clue that G/BN (7,7) could be the reasonable feature size for the ORR, considering both activity and efficiency. Therefore, G/BN (7,7) nanoribbon was selected as the optimal model to investigate the water formation and its release reactions.

Based on the results of our spin-polarized DFT-D calculations, the important geometrical parameters, binding energies, and charge transfer for the ORR on G/BN (7,7) nanoribbon are summarized in Table 2. Figure 4 shows the minimum energy pathway of O_2 adsorption on the G/BN nanoribbon, in which the most stable site for O_2 adsorption is the C-N interface.

Table 1. The important geometry parameters, bond distances (r) in Å, bond angles (α) in degrees, and binding energies (E_ad) in eV of chemisorption of O_2 on the C-N heterointerfaces of G/BN nanoribbons with different sizes, as well as the charge transfer (CT) in electron from G/BN to O_2 of these chemisorption configurations.

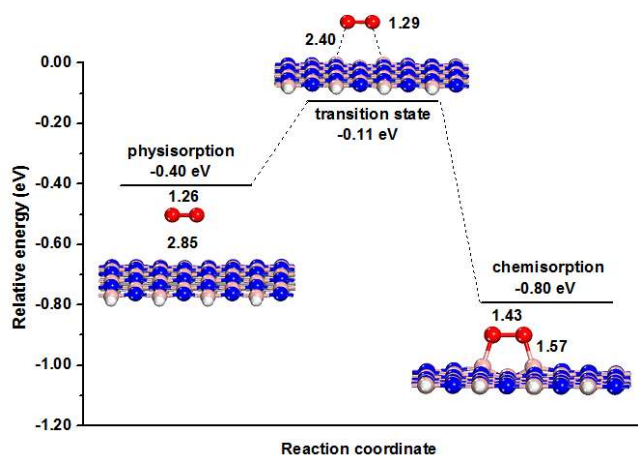| index	r(O–O)	r(O–B)	r(B–B)	α(O–O–B)	CT	E_ad
G/BN (3,3)	1.422	1.576	2.529	106.8	-0.475	0.59
G/BN (4,4)	1.427	1.572	2.330	106.7	-0.486	0.69
G/BN (5,5)	1.427	1.570	2.329	106.7	-0.490	0.75
G/BN (6,6)	1.431	1.567	2.331	106.7	-0.494	0.78
G/BN (7,7)	1.431	1.567	2.329	106.6	-0.496	0.80
G/BN (8,8)	1.432	1.568	2.330	106.6	-0.498	0.81
G/BN(9,9)	1.433	1.567	2.329	106.6	-0.498	0.82
G/BN (10,10)	1.434	1.566	2.330	106.6	-0.500	0.82

Figure 4. Reaction mechanism of O_2 adsorption on G/BN (7,7) nanoribbon. Atom color code: blue, nitrogen; pink, boron; gray, carbon; white, hydrogen.

Table 2. Binding energy (E_ad) in eV, bond distance (r) in Å, and bond angle (α) in deg. of O_2 adsorbed on G/BN (7,7), and the charge transfer (CT) in electron from G/BN to O_2 for these configurations.

	Physisorption	Transition state	Chemisorption
E_ad	-0.40	-0.11	-0.80
r(O–O)	1.262	1.292	1.431
r(B–O)	2.855	2.402	1.567
r(B–B)	2.484	2.462	2.329
α(O–O–B)	102.4	104.0	106.6
CT	0.258	0.381	0.496

The O_2 adsorption includes physisorption and chemisorption. In the case of physisorption, the O_2 molecule is quite far from the adsorption site, with a B…O distance of 2.855 Å and an binding energy of 0.40 eV. The interaction between the B and O atoms is relatively weak, and it mainly comes from the van der Waals interactions. The weak interaction is also supported by the small charge transfer between them. The charge transfer from the G/BN nanoribbon to O_2 is -0.002 e for the physisorbed configuration. In contrast, for the chemisorbed configuration, chemical bonds between O_2 and the G/BN nanoribbon (i.e. B-O bonds) are formed with a bond length of 1.567 Å. The O-O bond length is 1.431 Å, which is longer than the bond length in its gas phase (1.225 Å). The binding energy for the chemisorbed configuration is 0.80 eV. This strong interaction is
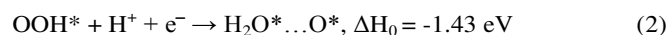
also supported by the large amount of charge transfer from the G/BN nanoribbon to the O_2 molecule (-0.496 e). The reaction pathway shows that the barrier from the physisorption to the chemisorption is 0.29 eV. These results demonstrate the adsorption of O_2 on the G/BN nanoribbon is exothermic with a low barrier, which means that the adsorption is thermodynamically feasible. It is well known that the criteria for materials with high catalytic activities at the cathode of hydrogen fuel cells are that the activation energies for the ORR and subsequent water formation reactions for the reduced O_2, H^+, and electron reactions should not be too high, and that the water molecules formed can be easily released from the active sites of these materials to keep the reaction site active. Nørskov provided models for ORR through computational study.[40] The above calculations reveal that the adsorption of O_2 on the C-N interface of G/BN nanoribbon is exothermic and has a low barrier, which satisfies the first criterion.

We now investigate the water formation and its subsequential release from the heterointerface of G/BN nanoribbon to further identify whether it is an efficient catalyst for ORR reactions. The calculated geometrical structures of the intermediates and products of water formation reactions on the interface of G/BN (7,7) nanoribbon and the potential energy surface of reactions are presented in Figures 5 and 6. Our calculations also indicate that O_2 dissociation reaction prior to H adsorption is energetic unfavourable (the detail information is listed in Figure S2 in the supporting information). After O_2 adsorption on top of the boron atoms at the heterointerface of G/BN nanoribbon, it can be reduced through either a two electron pathway ($2e^-$) to form hydrogen peroxide (HOOH) as the final product or a four-electron ($4e^-$) pathway to form water as the final product. The $4e^-$ pathway, which involves O-O bond breaking, is efficient and desirable for the G/BN patchwork in the fuel cell. The configuration of adsorbed O_2^* reacting with one H^+ and one e^- for the formation of OOH* on G/BN nanoribbon [Eq. (1)] is presented in Figure 5. We have valued the heat of reaction (ΔH_0) for each step in water formation reaction. ΔH_0 refers to the enthalpy difference between the reactant and the product of the reactions in water formation.

$$O_2^* + H^+ + e^- \rightarrow OOH^*, \Delta H_0 = -1.28 \text{ eV} \quad (1)$$
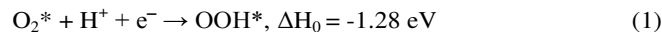
The optimized configuration shows that OOH* is adsorbed chemically on the C-N interface, and the most favourable adsorption site is where one boron atom connects with an O atom with a B-O bond length of 1.485 Å. The reaction for the formation of OOH* is exothermic with a value of 1.28 eV, which indicates that the reaction is favourable. The structure that H binds to the G/BN interface with chemisorbed O_2 is energy unfavourable, as demonstrated by Figure S3 in the supporting information.

The formed OOH* further reacts with H^+ and e^- to generate two configurations on the C-N interface through Eqs. (2) and (3).

$$OOH^* + H^+ + e^- \rightarrow H_2O^*…O^*, \Delta H_0 = -1.43 \text{ eV} \quad (2)$$

$$OOH^* + H^+ + e^- \rightarrow OH^*…OH^*, \Delta H_0 = -2.62 \text{ eV} \quad (3)$$

These two reactions [i.e., Eqs. (2) and (3)] are strongly exothermic, with values of 1.43 eV and 2.62 eV, respectively.

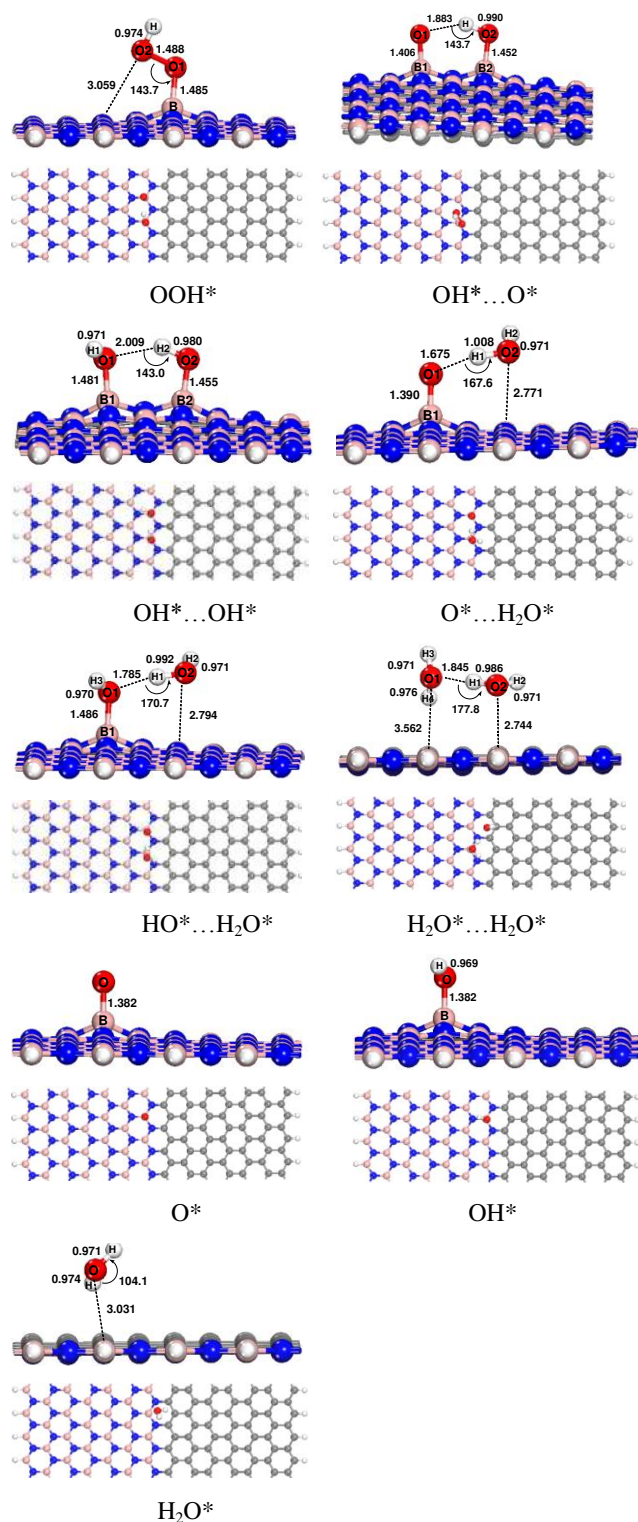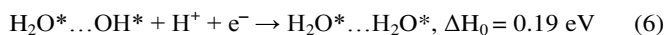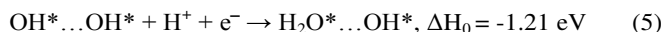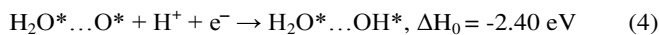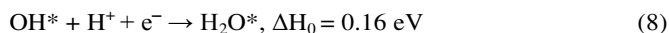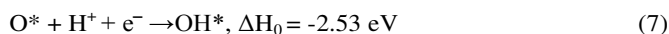**Figure 5.** Side and top views of the intermediates and products of water formation reactions on the heterointerface of G/BN (7,7) nanoribbon. The results show that OOH* is more likely to break the O-OH* bond along the pathway of hydrogenation dissociation, and then the water formation reaction is through four-electron pathway. By comparing the two reaction pathways of OOH* dissociation, we found that the reaction to form 2OH* is more exothermic

than the formation of H_2O^* and O^*. Therefore, 2OH* is the most favourable product of OOH* reduction. There are further reactions of the above two products with H+ and e-, which are summarized in Eqs. (4) and (5).

$$H_2O^* \cdots O^* + H^+ + e^- \rightarrow H_2O^* \cdots OH^*, \Delta H_0 = -2.40 \text{ eV} \qquad (4)$$

$$OH^* \cdots OH^* + H^+ + e^- \rightarrow H_2O^* \cdots OH^*, \Delta H_0 = -1.21 \text{ eV} \qquad (5)$$

$$H_2O^* \cdots OH^* + H^+ + e^- \rightarrow H_2O^* \cdots H_2O^*, \Delta H_0 = 0.19 \text{ eV} \qquad (6)$$

The reactions of Eq. (4) and Eq. (5) produce the same product, and they are exothermic with values of 2.40 eV and 1.21 eV, respectively. In the optimized $H_2O^* \cdots OH^*$ product, the O atom of OH* is directly connected with the boron atom of the C-N interface, with an O-B bond length of 1.486 Å. In addition, the O atom in the H_2O^* molecule forms a weak interaction with another boron atom, and their bond length is 2.794 Å. There is an O⋯HO hydrogen bond (where the hydrogen bond distance is 1.785 Å and the bond angle is 170.0º) in this product which connects the OH* and H_2O^* parts. The last step of water formation [Eq. (6)] is endothermic with a small value of 0.19 eV. Overall, the water formation reactions are feasible.

The reaction of O* with H⁺ and e⁻ to form OH*, is described in Eq. (7). The reaction is downhill with reaction energy of 2.53 eV. The formed OH* further reacts with H⁺ and e⁻ to produce water as shown in Eq. (8). Although this reaction is endothermic with a very small value of 0.16 eV, the formation reaction is still feasible.

$$O^* + H^+ + e^- \rightarrow OH^*, \Delta H_0 = -2.53 \text{ eV} \qquad (7)$$

$$OH^* + H^+ + e^- \rightarrow H_2O^*, \Delta H_0 = 0.16 \text{ eV} \qquad (8)$$

The release of the thus-formed water molecules was also investigated in order to gain information about the regeneration of active sites in G/BN nanoribbon. A desirable catalyst for the ORR should release the formed water easily to keep the reaction site active. The binding energy (BE) of one water and two water molecules with the nanoribbon through the intermediates H_2O^* and $H_2O^* \cdots H_2O^*$, respectively, was calculated via the following Eq. (9)

$$E_{BE} = (E_{G/BN} + nE_{H2O}) - E_{G/BN-nH2O^*} (n = 1 \text{ or } 2) \qquad (9)$$

The structure of intermediate H_2O^* is very close to its gas-phase structure, where the lengths of the two OH bonds are 0.971 Å and 0.974 Å, respectively, and the HOH bond angle of the formed water is 104.1º. The calculated OH bond lengths for the gas-phase H_2O are both 0.971 Å, and the HOH bond angle is 104.2º. The calculated distance between H_2O^* and the nanoribbon is 3.031 Å, and the above results indicate that the interaction between one H_2O and the G/BN nanoribbon is very weak and that it is mainly comes from the van der Waals interaction. The calculated binding energy between the formed water and the G/BN nanoribbon is 0.26 eV, which again supports the weak interactions between the water and the G/BN. We can draw the conclusion that the water formed in the ORR reaction can be easily released from the active sites of the nanoribbon, and they can be reused for the next catalytic reaction.

In the configuration of $H_2O^* \cdots H_2O^*$ (please see the structure of $H_2O^* \cdots H_2O^*$ in Figure 5) where two water molecules are

formed through the above reactions, the distances between the G/BN and the water molecules are quite far, and the bond lengths between them are 2.744 Å and 3.564 Å, respectively.

reduction involves the 4e⁻ pathway, not the 2e⁻ one. The formed water molecules can be easily released from the interface, and the active sites can be regenerated for next cycle
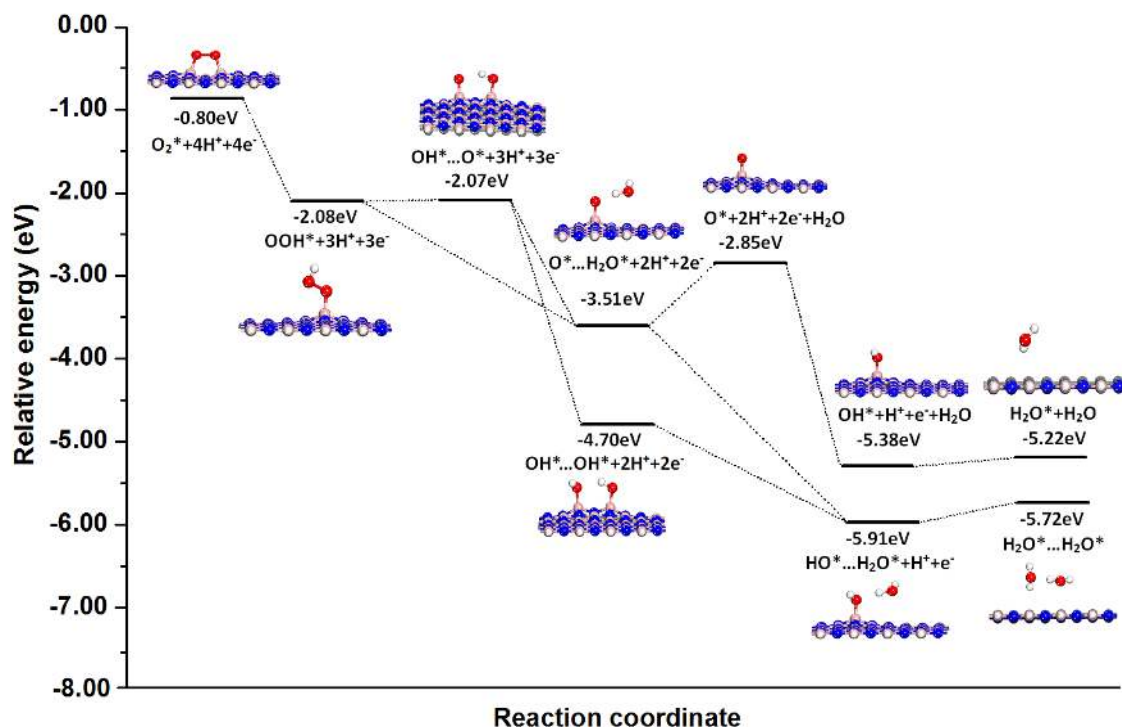

Figure 6. Reaction mechanism of water formation on the heterointerface of G/BN (7,7) nanoribbon.

Similar to the case of one water molecule interacting with the G/BN nanoribbon, the structures of the two water molecules are very similar to their gas-phase structures. The total binding energy is 0.76 eV, which includes the interactions between the two water molecules and the G/BN nanoribbon, and the interaction between the two water molecules through a relatively strong hydrogen bond (HO…H). Therefore, the average binding energy of two water molecules with G/BN is less than ~ 0.3 eV, and their interactions are very weak. Overall, the above results clearly indicate that in both cases of H_2O^* and $H_2O^*…H_2O^*$, the release of the water molecules from the active sites of the heterointerfaces from G/BN nanoribbon is feasible, and the interface can be kept active.

Conclusions

The orientation and size effects of the hybrid G/BN nanomaterials on the ORR were comprehensively investigated through spin-polarized DFT-D calculations. The results show that the C-N interfaces of G/BN nanoribbons can act as a source of active sites for the ORR, and that the G/BN (7,7) nanoribbon features the best activity and efficiency among different sized nanoribbons. The adsorption and reduction of O_2, and the formation and release of water on the G/BN nanoribbons were studied by using G/BN (7,7) nanoribbon as the optimal model. The results demonstrate that the oxygen

of the ORR. Our study provides significant insights in exploration of hybrid G/BN nanomaterials as novel, highly efficient, and metal-free catalysts in FCs.

Methods

First-principles density-functional theory plus dispersion (DFT-D) calculations were carried out using the DMol3 module in Materials Studio.[41, 42] The G/BN nanoribbons are fully optimized in the given symmetry using the generalized gradient approximation[43], treated by the Perdew-Burke-Ernzerhof exchange-correlation potential with long range dispersion correction via Grimme's scheme.[44] An all-electron double numerical atomic orbital augmented by d-polarization functions (DNP) is used as the basis set. This method has been used to successfully determine the interactions between some gases and boron nitride nanotubes, boron nitride nanosheets, boron carbon nanotubes, and boron nanomaterials.[45-48] The self-consistent field (SCF) procedure was used with a convergence threshold of 10^{-6} au on energy and electron density. The direct inversion of the iterative subspace technique developed by Pulay is used with a subspace size 6 to speed up SCF convergence on these systems.[49] Starting with all possible configurations of the O_2 adsorbed on the G/BN nanoribbons, geometry optimizations were performed with a convergence threshold of 0.002 au/Å on the gradient, 0.005 Å on the displacement, and 10^{-5} au on the energy. The real-space global cut-off radius is set to be 4.10 Å.

Hydrogen atoms are added to the edge atoms to saturate the G/BN nanoribbons. For G/BN nanoribbons, tetragonal supercells with dimensions of $50 \times 15 \times c$ Å^3 are used, where the optimized c parameter is approximately in the range of 9.944 Å to 9.956 Å depending on the size of the nanoribbon G/BN (n,n), where n is from 3 to 10 and represents the numbers of unit cells of graphene and BN. A 15 Å vacuum between the nanoribbons and a 50 Å length of the supercell are large enough to avoid interactions between periodic images. The optimized lengths of the nanoribbons, including the saturated hydrogen atoms, are 13.771 Å, 18.093 Å, 22.414 Å, 26.731 Å, 31.051 Å, 35.374 Å, 39.694 Å, and 44.013 Å for G/BN (3,3), G/BN (4,4), G/BN (5,5), G/BN (6,6), G/BN (7,7), G/BN (8,8), G/BN (9,9), and G/BN (10,10), respectively. The Brillouin zones are sampled by $1 \times 1 \times 6$ k-points using the Monkhorst-Pack scheme for these G/BN nanoribbons. The accurate band structure calculations are preformed by using 50 k-points along the Z-axis.

The binding energies of O_2 adsorption on G/BN nanoribbons are calculated from Eq. (10).

$$E_{ad} = (E_{G/BN} + E_{O2}) - E_{G/BN-O2} \tag{10}$$

where $E_{G/BN-O2}$ is the total energy of the G/BN nanomaterials with the adsorbed O_2, $E_{G/BN}$ is the energy of the isolated G/BN nanoribbon, and E_{O2} is the energy of an isolated O_2 molecule. The complete LST (linear synchronous transit)/QST (quadratic synchronous transit) method[50] implemented in the DMol3 code is used to find the transition states between reactant and product. Electron distributions and transfer mechanisms are determined by the Mulliken method.[51]

Acknowledgements

Notes and references

[a] Collaborative Innovation Center of Radiation Medicine of Jiangsu Higher Education Institutions, School of Radiation Medicine and Protection, Medical College of Soochow University, Soochow University, Suzhou 215123, China. Email: zhenli@suda.edu.cn

[b] Key Laboratory for Ultrafine Materials of the Ministry of Education, Shanghai Key Laboratory of Advanced Polymeric Materials, School of Materials Science and Engineering, East China University of Science and Technology, Shanghai 200237, China.

[c] School of Chemistry, Physics and Mechanical Engineering, Queensland University of Technology, Brisbane, QLD 4001, Australia.

[d] Institute of Superconducting & Electronic Materials, The University of Wollongong, NSW 2500, Australia. Email: zhenl@uow.edu.au

1. B. C. H. Steele and A. Heinzel, *Nature*, 2001, **414**, 345.
2. H. A. Gasteiger and N. M. Markovic, *Science*, 2009, **324**, 48.
3. R. Bashyam and P. Zelenay, *Nature*, 2006, **443**, 63.
4. K. Gong, F. Du, Z. Xia, M. Durstock and L. Dai, *Science*, 2009, **323**, 760.
5. A. K. Geim, *Science*, 2009, **324**, 1530.
6. K. S. Novoselov, A. K. Geim, S. V. Morozov, D. Jiang, Y. Zhang, S. V. Dubonos, I. V. Grigorieva and A. A. Firsov, *Science*, 2004, **306**, 666.
7. K. S. Novoselov, A. K. Geim, S. V. Morozov, D. Jiang, M. I. Katsnelson, I. V. Grigorieva, S. V. Dubonos and A. A. Firsov, *Nature*, 2005, **438**, 197.
8. M. P. Levendorf, C.-J. Kim, L. Brown, P. Y. Huang, R. W. Havener, D. A. Muller and J. Park, *Nature*, 2012, **488**, 627.
9. Y. Kubota, K. Watanabe, O. Tsuda and T. Taniguchi, *Science*, 2007, **317**, 932.
10. M. Corso, W. Auwarter, M. Muntwiler, A. Tamai, T. Greber and J. Osterwalder, *Science*, 2004, **303**, 217.
11. N. G. Chopra, R. J. Luyken, K. Cherrey, V. H. Crespi, M. L. Cohen, S. G. Louie and A. Zettl, *Science*, 1995, **269**, 966.
12. S. Wang, L. Zhang, Z. Xia, A. Roy, D. W. Chang, J.-B. Baek and L. Dai, *Angew. Chem. Int. Ed.*, 2012, **51**, 4209.
13. S. Wang, E. Iyyamperumal, A. Roy, Y. Xue, D. Yu and L. Dai, *Angew. Chem. Int. Ed.*, 2011, **50**, 11756.
14. F. Gao, G.-L. Zhao, S. Yang and J. J. Spivey, *J. Am. Chem. Soc.*, 2013, **135**, 3315.
15. Y. Tang, B. L. Allen, D. R. Kauffman and A. Star, *J. Am. Chem. Soc.*, 2009, **131**, 13200.
16. D. Yu, Q. Zhang and L. Dai, *J. Am. Chem. Soc.*, 2010, **132**, 15127.
17. Y. Zhao, L. J. Yang, S. Chen, X. Z. Wang, Y. W. Ma, Q. Wu, Y. F. Jiang, W. J. Qian and Z. Hu, *J. Am. Chem. Soc.*, 2013, **135**, 1201.
18. L. Yang, S. Jiang, Y. Zhao, L. Zhu, S. Chen, X. Wang, Q. Wu, J. Ma, Y. Ma and Z. Hu, *Angew. Chem. Int. Ed.*, 2011, **50**, 7132.
19. J. Jin, F. Pan, L. Jiang, X. Fu, A. Liang, Z. Wei, J. Zhang and G. Sun, *ACS Nano*, 2014, **8**, 3313.
20. K. Yan, H.-W. Lee, T. Gao, G. Zheng, H. Yao, H. Wang, Z. Lu, Y. Zhou, Z. Liang, Z. Liu, S. Chu and Y. Cui, *Nano Lett.*, 2014, **14**, 6016.
21. T. Ikeda, M. Boero, S.-F. Huang, K. Terakura, M. Oshima, J.-i. Ozaki and S. Miyata, *J. Phys. Chem. C*, 2010, **114**, 8933.
22. L. Ferrighi, M. Datteo and C. Di Valentin, *J. Phys. Chem. C*, 2014, **118**, 223.
23. K. Uosaki, G. Elumalai, H. Noguchi, T. Masuda, A. Lyalin, A. Nakayama and T. Taketsugu, *J. Am. Chem. Soc.*, 2014, **136**, 6542.
24. H. Zeng, C. Zhi, Z. Zhang, X. Wei, X. Wang, W. Guo, Y. Bando and D. Golberg, *Nano Lett.*, 2010, **10**, 5049.
25. Q. Li, M. Liu, Y. Zhang and Z. Liu, *Small*, 2016, **12**, 32.
26. L. Ci, L. Song, C. Jin, D. Jariwala, D. Wu, Y. Li, A. Srivastava, Z. F. Wang, K. Storr, L. Balicas, F. Liu and P. M. Ajayan, *Nat. Mater.*, 2010, **9**, 430.
27. J. Lu, K. Zhang, X. F. Liu, H. Zhang, T. C. Sum, A. H. Castro Neto and K. P. Loh, *Nat. Commun.*, 2013, **4**, 2681.
28. L. Liu, J. Park, D. A. Siegel, K. F. McCarty, K. W. Clark, W. Deng, L. Basile, J. C. Idrobo, A.-P. Li and G. Gu, *Science*, 2014, **343**, 163.
29. R. Drost, A. Uppstu, F. Schulz, S. K. Hamalainen, A. Harju and P. Liljeroth, *Nano Lett.*, 2014, **14**, 5128.
30. Y. Gao, Y. Zhang, P. Chen, Y. Li, M. Liu, T. Gao, D. Ma, Y. Chen, Z. Cheng, X. Qiu, W. Duan and Z. Liu, *Nano Lett.*, 2013, **13**, 3439.
31. Y. Liu, S. Bhowmick and B. I. Yakobson, *Nano Lett.*, 2011, **11**, 3113.
32. J. Lu, L. C. Gomes, R. W. Nunes, A. H. Castro Neto and K. P. Loh, *Nano Lett.*, 2014, **14**, 5133.
33. M. Liu, Y. Li, P. Chen, J. Sun, D. Ma, Q. Li, T. Gao, Y. Gao, Z. Cheng, X. Qiu, Y. Fang, Y. Zhang and Z. Liu, *Nano Lett.*, 2014, **14**, 6342.
34. B. Muchharla, A. Pathak, Z. Liu, L. Song, T. Jayasekera, S. Kar, R. Vajtai, L. Balicas, P. M. Ajayan, S. Talapatra and N. Ali, *Nano Lett.*, 2013, **13**, 3476.
35. P. Sutter, Y. Huang and E. Sutter, *Nano Lett.*, 2014, **14**, 4846.

36. Z. Liu, L. Ma, G. Shi, W. Zhou, Y. Gong, S. Lei, X. Yang, J. Zhang, J. Yu, K. P. Hackenberg, A. Babakhani, J.-C. Idrobo, R. Vajtai, J. Lou and P. M. Ajayan, *Nat. Nanotechnol.*, 2013, **8**, 119.
37. S. J. Kang, G.-H. Lee, Y.-J. Yu, Y. Zhao, B. Kim, K. Watanabe, T. Taniguchi, J. Hone, P. Kim and C. Nuckolls, *Adv. Funct. Mater.*, 2014, **24**, 5157.
38. R. S. Krsmanovic and Z. Sljivancanin, *J. Phys. Chem. C*, 2014, **118**, 16104.
39. S. Nappini, I. Pis, T. O. Mentes, A. Sala, M. Cattelan, S. Agnoli, F. Bondino and E. Magnano, *Adv. Funct. Mater.*, 2016, **26**, 1120.
40. J. K. Norskov, J. Rossmeisl, A. Logadottir, L. Lindqvist, J. R. Kitchin, T. Bligaard and H. Jonsson, *J. Phys. Chem. B*, 2004, **108**, 17886.
41. B. Delley, *J. Chem. Phys.* , 1990, **92**, 508.
42. B. Delley, *J. Chem. Phys.* , 2000, **113**, 7756.
43. J. P. Perdew, K. Burke and M. Ernzerhof, *Phys. Rev. Lett.*, 1996, **77**, 3865.
44. S. Grimme, *J. Comput. Chem.*, 2006, **27**, 1787.
45. Q. Sun, M. Wang, Z. Li, A. Du and D. J. Searles, *J. Phys. Chem. C*, 2014, **118**, 2170.
46. Q. Sun, M. Wang, Z. Li, A. Du and D. J. Searles, *Phys. Chem. Chem. Phys.*, 2014, **16**, 12695.
47. Q. Sun, Z. Li, D. J. Searles, Y. Chen, G. Q. Lu and A. J. Du, *J. Am. Chem. Soc.*, 2013, **135**, 8246.
48. X. Wu, W. An and X. C. Zeng, *J. Am. Chem. Soc.*, 2006, **128**, 12001.
49. P. Pulay, *J. Comput. Chem.* , 1982, **3**, 556.
50. T. A. Halgren and W. N. Lipscomb, *Chem. Phys. Lett.*, 1977, **49**, 225.
51. R. S. Mulliken, *J. Chem. Phys.*, 1955, **23**, 1833.